JMEPEG (2012) 21:1970–1977
DOI: 10.1007/s11665-011-0110-2

1059-9495/$19.00

Effect of Rotating Magnetic Field (RMF) on Segregation of Solute Elements in CuNi10Fe1Mn Alloy Hollow Billet

Zhiming Yan, Wenzhong Jin, and Tingju Li

(Submitted May 17, 2011; in revised form November 9, 2011)

The effect of rotating magnetic field (RMF) on macro/microsegregation of solute elements is investigated experimentally, and a comprehensive three-dimensional mathematical model is built, and the finite element package ANSYS® is employed to calculate the distribution of temperature and liquid fraction along the radial direction in horizontal continuous casting of CuNi10Fe1Mn alloy hollow billet. The results show that RMF makes the temperature field and liquid fraction uniform. The original inhomogeneous columnar grain macrostructure turns into homogeneous equiaxed grain structure, and the macro/microsegregation of Ni, Fe, and Mn elements are restrained effectively with the application of RMF. Moreover, the action mechanism of RMF is discussed to explain its effect on improving the distribution of solute elements.

Keywords CuNi10Fe1Mn alloy, horizontal continuous casting, rotating magnetic field (RMF), segregation

1. Introduction

CuNi10Fe1Mn alloy which has excellent corrosion resistance and mechanical properties is widely used as cooling-condition material in shipping and electric power industry (Ref 1). However, in conventional horizontal continuous casting, the distribution of solute elements in CuNi10Fe1Mn alloy presents severe segregation which has bad influence on the subsequent procedures (Ref 2). Therefore, it is urgent to reduce the segregation of the solute elements.

With reference to quality, segregation—an inhomogeneous distribution of alloying elements on different length scales—is characteristic of all the cast products (Ref 3). Based on the scale of the segregation phenomena, it may be divided into two parts: macrosegregation and microsegregation. Macrosegregation is an inhomogeneous distribution of alloying elements on the scale of the casting (Ref 4, 5). Microsegregation includes short-range differences in chemical composition, such as those found between cells, dendrites, and grains. Many researchers have paid more attention to segregation phenomena in vertical continuous casting of aluminum and magnesium alloys by experimental and numerical simulation (Ref 3-8).

It has been demonstrated that the melt acted by rotating magnetic field (RMF) has the advantages of refining solidification structure, reducing segregation and shrinkage cavity (Ref 9, 10). RMF has been successfully applied to horizontal continuous casting of copper and copper alloy hollow billets (Ref 11, 12), whereas few studies have been done to research on the effect of RMF on macro/microsegregation of solute elements in CuNi10Fe1Mn alloy hollow billet.

For better use of electromagnetic field, researchers pay special attention to the simulation of the same. Zheng et al. (Ref 13) built a three-dimensional non-steady homogeneous heat-transfer equation to numerically simulate the temperature field during the electromagnetic semi-continuous casting of slab. Natarajan et al. (Ref 14) used an efficient finite element segregated algorithm to simulate the electromagnetic field and fluid flow phenomena in sub-mold rotary electromagnetic stirring in continuous casting of steel.

In the horizontal electromagnetic continuous casting process, the graphite mold and the holding furnace are directly connected. Hence, the flow behavior of the melt under electromagnetic field cannot be measured directly. Li et al. (Ref 15) used a two-dimensional model to simulate the influence of casting temperature, cooling intensity and casting speed on the mushy zone width and the sump depth during horizontal continuous casting process of BFe30-1-1 hollow billets. However, few numerical simulation studies have been done to investigate the effect of RMF on the horizontal continuous casting process of CuNi10-Fe1Mn alloy hollow billet.

This article investigates the effect of RMF on macro/microsegregation of solute elements, and builds a comprehensive three-dimensional mathematical model and uses the finite element package ANSYS® to calculate the distribution of temperature and liquid fraction along the radial direction in horizontal continuous casting of CuNi10Fe1Mn alloy hollow billet.

2. Experimental

2.1 Experimental Apparatus

The experimental apparatus, which consists of the commercial frequency furnace, crystallizer, drawing system, and electromagnetic system, is shown in Fig. 1. The crystallizer is composed of a graphite mold and a copper outer-jacket. The

Zhiming Yan, School of Materials Science and Engineering, Dalian Jiaotong University, Dalian 116028, China; **Wenzhong Jin**, Department of Mechanical and Electronic Engineering, Luoyang Institute of Science and Technology, Luoyang 471023, China; and **Tingju Li**, School of Materials Science and Engineering, Dalian University of Technology, Dalian 116085, China. Contact e-mail: zmyan1981@yahoo.com.cn.

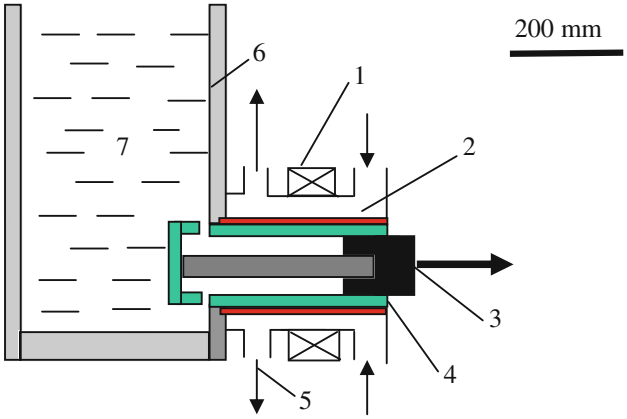

Fig. 1 Schematic view of horizontal electromagnetic continuous casting apparatus: (1) RMF generator, (2) cooling system, (3) drawing system, (4) graphite mold, (5) cooling water, (6) furnace, and (7) molten metal

Table 1 Nominal composition of CuNi10Fe1Mn alloy (wt.%)

Elements	Ni	Fe	Mn	Cu
Composition	10.0	1.4	1.0	Balance

length of graphite mold is 385 mm, and the taper of its inner core is 1°. RMF is generated by the three-phase-three-pole induced coil outside the graphite mold.

2.2 Experimental Materials and Process

The nominal composition of CuNi10Fe1Mn alloy is shown in Table 1. The specimens selected along the transverse section for macrostructures were polished and etched by a solution of 50 mL HNO_3 and 50 mL H_2O, while for microstructures were polished and etched by a solution of 3 g $FeCl_3$, 4 mL HCl and 96 mL C_2H_5OH. X-ray fluorescence spectrometer (XRF, XRF-1800) and Electron Probe Micro-Analyzer (EPMA, EPMA-1600) were employed to analyze the macrosegregation and microsegregation of solute elements, respectively.

3. Mathematical Model

3.1 Basic Assumptions

In order to simplify the mathematical model, some assumptions are given as follows:

(1) The melt behaves as an incompressible Newtonian liquid;
(2) The variety of the flow field has little effect on the distribution of the electromagnetic field, because the magnetic Reynolds number $R_m \ll 1$. Base on Ohm's Law ($\vec{J} = \sigma(\vec{E} + \vec{U} \times \vec{B})$, the second term of right-hand side of this equation ($\vec{U} \times \vec{B}$)) is ignored;
(3) The displacement current $\partial D/\partial t$ is neglected, because the melt is sufficiently conducting body in which the charge relaxation time is shorter than the transit time of electromagnetic waves. Therefore, the Ampere's law can be simplified as $\nabla \times \vec{B} = \mu\vec{J}$.

3.2 Governing Equations for Electromagnetic Field

Gauss's law of magnetic field: $\nabla \times \vec{B} = 0$ (Eq 1)

Ampere's law: $\nabla \times \vec{B} = \mu\vec{J}$ (Eq 2)

Faraday's law: $\nabla \times \vec{E} = -\dfrac{\partial \vec{B}}{\partial t}$ (Eq 3)

Ohm's law: $\vec{J} = \sigma\vec{E}$ (Eq 4)

where σ is the electric conductivity; and μ is the permeability, $\vec{B}$ is the magnetic flux density; $\vec{E}$ is the electric field strength, and $\vec{J}$ is the current density.

The electromagnetic force density for each element is calculated by the relationship:

$$\vec{F}_{em} = \vec{J} \times \vec{B} \quad \text{(Eq 5)}$$

The time-averaged electromagnetic force in the induced electromagnetic field can be described by the following equation:

$$\vec{F} = \frac{1}{2}\mathrm{Re}(\vec{J} \times \vec{B}) \quad \text{(Eq 6)}$$

where Re is the real part of a complex quantity.

3.3 Governing Equations for Flow Field

Continuity equation: $\dfrac{\partial(\rho u_i)}{\partial x_i} = 0$ (Eq 7)

Momentum equation: $$\frac{\partial(\rho u_i)}{\partial t} + \frac{\partial(\rho u_i u_j)}{\partial x_i} = \rho g_i - \frac{\partial p}{\partial x_i} + \frac{\partial}{\partial x_i}(\mu_{\mathrm{eff}} \frac{\partial u_i}{\partial x_i}) + F_i \quad \text{(Eq 8)}$$

where ρ is the density of melt; u_i, u_j are the time average velocities; p is the pressure; μ_{eff} is the effective viscosity coefficient, $\mu_{\mathrm{eff}} = \mu_l + \mu_t$; μ_l is the laminar viscosity; μ_t is the turbulent viscosity; g_i is the gravitational acceleration; F_i is the momentum of source including the thermal buoyancy and the time-averaged electromagnetic force.

The standard k-ε model, which is a semi-empirical model, is used to describe the transport of turbulence kinetic energy (k) and its dissipation rate (ε). The first form of this model is

$$\mu_t = \rho C_\mu \frac{k^2}{\varepsilon} \quad \text{(Eq 9)}$$

where C_μ is a function of the turbulent Reynolds number that is a constant value; k and ε are the turbulence kinetic energy and its dissipation rate, respectively, and can be obtained from the following transport equations:

Turbulent kinetic energy equation

$$\frac{\partial(\rho k)}{\partial t} + \frac{\partial(\rho u_i k)}{\partial x_i} = \frac{\partial}{\partial x_i}\left[\left(\mu_l + \frac{\mu_t}{\sigma_k}\right)\frac{\partial k}{\partial x_i}\right] + G - \rho\varepsilon \quad \text{(Eq 10)}$$

where $G = u_t \frac{\partial u_i}{\partial x_j}\left(\frac{\partial \mu_i}{\partial x_j} + \frac{\partial \mu_j}{\partial x_i}\right)$; $\sigma_k = 1.0$.

Dissipation rate of turbulent kinetic energy

$$\frac{\partial(\rho\varepsilon)}{\partial t}+\frac{\partial(\rho u_i\varepsilon)}{\partial x_i}=\frac{\partial}{\partial x_i}\left[\left(\mu_l+\frac{\mu_t}{\sigma_\varepsilon}\right)\frac{\partial\varepsilon}{\partial x_i}\right]+c_1\frac{\varepsilon}{k}G-c_2\rho\frac{\varepsilon^2}{k} \quad \text{(Eq 11)}$$

where $c_1 = 1.44$; $c_2 = 1.92$; $c_\mu = 0.09$; $\sigma_k = 1.0$; $\sigma_\varepsilon = 1.3$ (Ref 16).

3.4 Governing Equations for Temperature Field

Energye quation: $\frac{\partial}{\partial t}(\rho H)+\nabla\cdot(\rho\vec{v}H)=\nabla\cdot(k_{\text{eff}}\nabla T)+S_h$ (Eq 12)

The enthalpy of the material is computed as the sum of the sensible enthalpy, $h = h_{\text{ref}} + \int_{T_{\text{ref}}}^{T} c_p dT$, and the latent heat, $\Delta H = f_L \Delta H_f$, in the energy equation as

$$H = h + \Delta H = \int_{T_{\text{ref}}}^{T} c_p dT + f_L \Delta H_f,$$

$$f_L = \begin{cases} 1 & T > T_L \\ \frac{T-T_S}{T_L-T_S} & T_S \le T \le T_L \\ 0 & T < T_S \end{cases}, \quad \text{(Eq 13)}$$

where $\vec{v}$ is the flow velocity; k_{eff} is the effective thermal conductivity; $k_{\text{eff}} = k + k_t$, k_t is the turbulent thermal conductivity; S_h is the thermal source including joule heat and latent heat of solidification; h_{ref} is the reference enthalpy; T_{ref} is the reference temperature; c_p is the specific heat at constant pressure; ΔH_f is the latent heat of solidification; f_L is the liquid fraction; and T_L and T_S are the liquidus and solidus temperatures, respectively.

The latent heat is released uniformly between the liquidus and solidus temperatures. In other words, the enthalpy changes linearly over the solidification range. The release of latent heat within the mushy region is properly incorporated in the energy equation as a source term.

3.5 Thermal Boundary Conditions

3.5.1 Inlet Boundary Condition. Set the internal surface of hollow billet as the velocity inlet boundary. The uniform profile for all variables is used at the surface as follows:

$$w = w_{\text{in}},\ u = v = 0,\ T = T_{\text{in}},\ k = 0.01 w_{\text{in}}^2,\ \varepsilon = \frac{C_\mu k^{1.5}}{0.05D} \quad \text{(Eq 14)}$$

where w_{in} is the inlet velocity, T_{in} is the casting temperature, and D is the hydraulic diameter of the inlet.

3.5.2 Outlet Boundary Condition. At the outlet, the condition of fully developed flow is adopted; normal gradients of all variables are set to zero.

3.5.3 Mold Wall. A non-slip condition and standard wall lows were applied for the internal surface and external surface of hollow billet.

In the stable stage, the temperature between the graphite mold and the internal surface is approximately equal, and no heat dissipates from the graphite mold, and therefore, set the internal surface as adiabatic boundary:

$$-k\frac{\partial T}{\partial n} = 0 \quad \text{(Eq 15)}$$

The external surface of hollow billet is the Neumann boundary conditions:

$$-k\frac{\partial T}{\partial n} = \bar{q} \quad \text{(Eq 16)}$$

During the horizontal continuous casting process, the heat conducted by the cooling copper sleeve is equal to the heat that is exported by the cooling water. Therefore, the average heat flux can be obtained by the equation:

$$\bar{q} = \frac{Q_w C_w \Delta T_w}{A} \quad \text{(Eq 17)}$$

where $\bar{q}$ is the average heat flux, Q_w is the cooling water quantity, C_w is the specific heat of water, ΔT is the temperature difference, and A is the effective cooling area.

3.6 Numerical Procedure and the Coupling Scheme for Multi Fields

Figure 2 shows the finite element model including the CuNi10Fe1Mn alloy hollow billet, the RMF generator that consisted of three pairs of coils and an iron core, the graphite mold, and cooling copper sleeve. However, the air around the RMF generator is omitted to show the details of the device. The size of hollow billet is ∅ 83 × 21 mm with a simulation length of 385 mm. The model contains about 230000 elements. The electromagnetic properties are listed in Table 2. Thermophysical, electrical and casting parameters are shown in Table 3. In addition, the origin of coordinates is in the center of RMF generator, as seen in Fig. 2.

In order to simulate the horizontal continuous casting process acted by RMF, the coupled modeling of electromagnetic field with other fields must be carried out. Based on the second item of assumptions, the electromagnetic field has effect on other fields but other fields have no effect on electromagnetic field. The governing equation of electromagnetic field is solved by ANSYS®. The obtained time average electromagnetic force (Eq 6) and Joule heat (Eq 17) are added to momentum equation and energy equation, respectively as source terms.

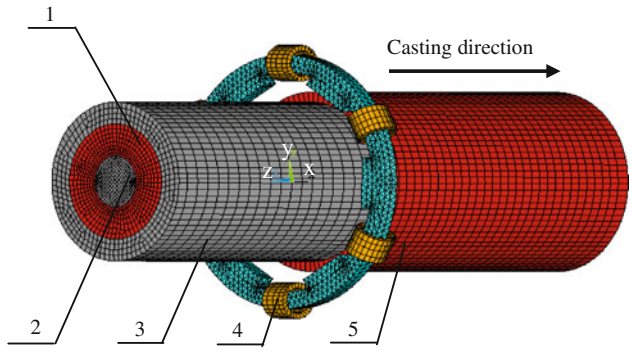

Fig. 2 Finite element model: (1) hollow billet, (2) internal surface of graphite mold, (3) external surface of graphite mold, (4) RMF generator, and (5) cooling copper sleeve

Table 2 Electromagnetic properties

Materials	Relative permeability (μ)	Electrical conductivity (σ), S m^{-1}
Air	1	…
Copper	1	4.93×10^7
Graphite	1	7.04×10^4
Iron core	7000	2.27×10^6
Coils	1	5.96×10^7
Copper (cooling copper sleeve)	1	3.33×10^7

Table 3 Thermo-physical, electrical and casting parameters

Parameters	Value
Density (ρ), kg m^{-3}	8900
Specific heat (c_p), J kg^{-1} K^{-1}	377
Thermal conductivity (k), W m^{-1} K^{-1}	46.1
Liquidus temperature (T_L), °C	1150
Solidus temperature (T_S), °C	1100
Latent heat of fusion (L), J kg^{-1}	212000
Viscosity (μ), m^2 s^{-1}	3.53×10^{-3}
Casting temperature (T_{in}), °C	1230
Casting speed, m s^{-1}	0.0058
Drawing time, s	0.5
Pausing time, s	0.4
Reversing time, s	0.2
Pausing time, s	0.4
Current intensity, A	120
Magnetic induction at internal surface of coil, mT	28.5
Magnetic induction at the center of coil, mT	22.3
Electromagnetic frequency, Hz	50

4. Results and Discussion

4.1 Effect of RMF on Solidification Structures of CuNi10Fe1Mn Alloy Hollow Billets

The effect of RMF on solidification structures of CuNi10-Fe1Mn alloy hollow billets is shown in Fig. 3. During horizontal continuous casting, only free convection exists in the melt which leads to high temperature gradient in radial direction and growth of columnar grains. On the bottom area, the hollow billet rests on the lower area of the internal wall of graphite mold under its own gravity, thus permitting good heat dissipation. On the top area, gap, which forms between the initial solidification shell and graphite mold due to solidification contraction, affects heat dissipation (Ref 11). Therefore, the macrostructure is inhomogeneous in the transverse section, which reveals a division into a top area of fine columnar grains and a region of coarse columnar grains at the bottom area of the hollow billet due to non-uniform heat dissipation, as shown in Fig. 3(a). The columnar grains grow approximately parallel to the direction of heat flow from the chilled external surface to internal surface. After the imposition of RMF, the original inhomogeneous columnar grain macrostructure changes into homogeneous equiaxed grain structure, as shown in Fig. 3(b).

The microstructures of CuNi10Fe1Mn alloy are shown in Fig. 3(c)-(f), where the selected areas are all at bottom areas without and with RMF. The microstructures without RMF are dendrites from external surface to internal surface. The primary dendrites at external surface have obvious orientation and secondary dendrite arm spacings are small, as shown in Fig. 3(c), and at internal surface, the average length of primary dendrites decreases, and secondary dendrite arm's spacings increase, as shown in Fig. 3(e). The microstructures with RMF from external surface to internal surface display the evolution from disordered dendrites without orientation to spherical grains. The primary dendrites do not have obvious orientation and their average lengths decrease obviously, and the secondary dendrite arm's spacings at external surface decrease, as shown in Fig. 3(d). The microstructure at internal surface which is similar to the spherical grain of rheocasting is refined and uniform, as shown in Fig. 3(f).

When alternating current is imposed, the coil generates a RMF in the melt. This field, in turn, creates an induced eddy current in the melt in opposite phase to the imposed alternating current. As a result, the melt is subjected to electromagnetic body force caused by the interaction of the eddy current and RMF. The Lorentz force density is expressed as follows (Ref 17):

$$F = J \times B = (1/\mu)(\nabla \times B) \times B \qquad \text{(Eq 18)}$$

where J is the induced eddy current; B and μ represent the electromagnetic flux density and electromagnetic permeability, respectively; ∇ is the Hamilton operator.

Figure 4 shows the effect of RMF on the distribution of temperature along the radial direction in hollow billet calculated by ANSYS®. As seen in the case of RMF, the electromagnetic body force takes the low-temperature melt near the external surface toward internal surface, the temperature field becomes very uniform and the temperature gradient between the external surface and internal surface is greatly reduced.

Figure 5 shows the effect of RMF on liquid fraction distribution along the radial direction in hollow billet calculated by ANSYS®. It can be seen that without RMF the slope of the solidification front is much steeper, and with RMF, the mushy region width is greatly increased. In addition, without RMF, the liquid fraction in the sump at the cross section is in the range from 0.33 to 1.0, and with RMF, this value range changes from 0.59 to 0.87. Since cooling the hollow billet mainly depends on the external surface, it is also observed that the melt close to the internal surface can hardly form initial solidification shell in the case without RMF.

The compulsive convection caused by RMF generates shearing force and plenty of dendrites are broken off. The dendrites on the solid-liquid interface are disturbed by the temperature fluctuation, and the necks of the dendrites are easy to be melted off. The dendrites which are melted off and broken off are distributed uniformly in the melt by RMF and serve as nucleus, so the nucleation rate increases.

With the application of RMF, the nucleation rate increases, while the temperature gradient reduces the one that promotes the transformation from columnar to equiaxed grains, and the grains grow in a uniform condition. The crystallization takes place simultaneously which causes the formation of a fine and homogeneous structure over the cross-section.

Owing to the different effects of cooling water on solidification from external surface to internal surface, the microstructure without RMF transforms from well-oriented dendrites

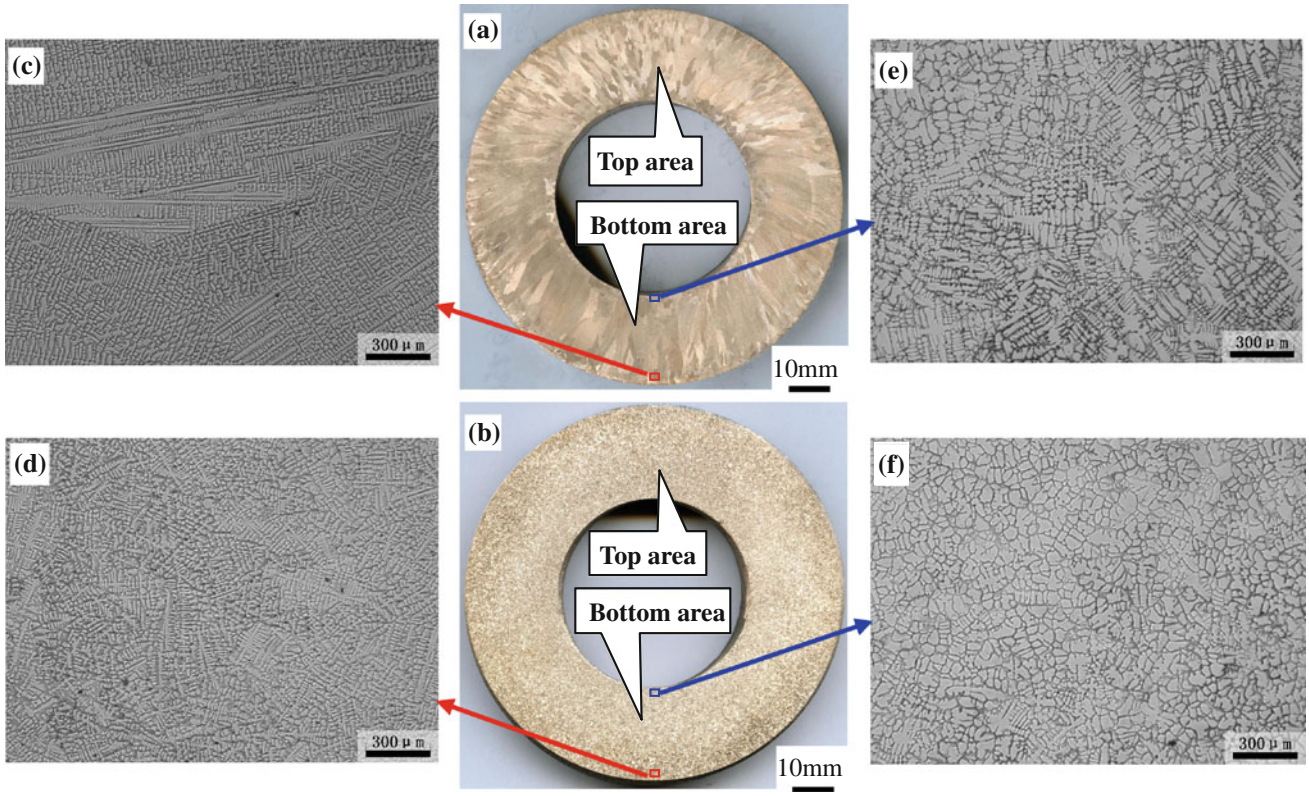

Fig. 3 Effect of RMF on solidification structures of CuNi10Fe1Mn alloy hollow billets: without RMF: (a) macrostructure, (c) microstructure at external surface, and (e) microstructure at internal surface; with RMF, I = 120 A: (b) macrostructure, (d) microstructure at external surface, and (f) microstructure at internal surface

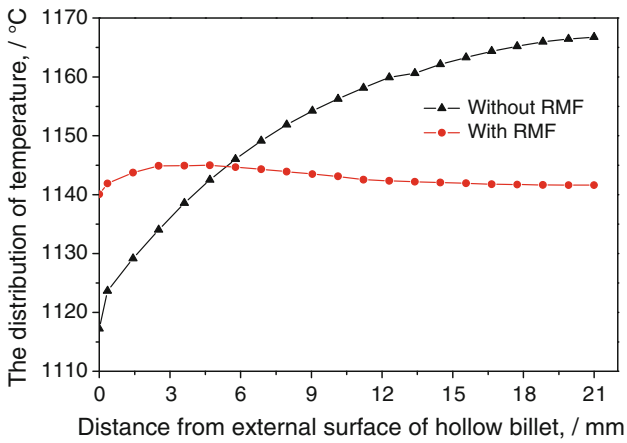

Fig. 4 Effect of RMF on the distribution of temperature along the radial direction of hollow billet

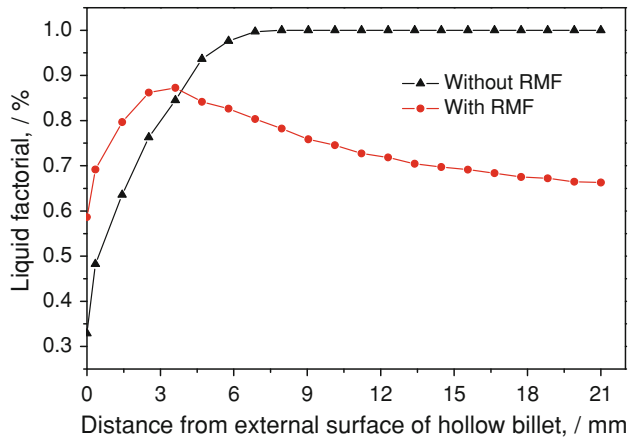

Fig. 5 Effect of RMF on the distribution of liquid fraction along the radial direction of hollow billet

to disordered ones. With the stirring effect of RMF, the temperature and concentration field of the internal melt are quite uniform. The remelted and fragmented dendrites offer nucleus and promote the microstructure to grow in equiaxed shape.

4.2 Effect of RMF on Macrosegregation of Solute Elements

The effect of RMF on macrosegregation of solute elements in radial direction of CuNi10Fe1Mn alloy hollow billet is tested by x-ray fluorescence spectrometer, as shown in Fig. 6. The distributions of Ni, Fe, and Mn elements show positive segregations from external surface to internal surface. Without RMF, the distributions over the transverse section are significantly inhomogeneous. The solute elements are highly enriched at the external surface, while the contents near the internal surface are lower than the average values. However, with the application of RMF, the concentration gradients of solute elements are significantly reduced and the distributions are quite uniform throughout the hollow billet.

For a given alloy, macrosegregation is linked to a variety of structural parameters, such as the morphology of the forming solid phase, magnitude of solidification shrinkage, level of solute rejection to the melt, and movement of the solid phase in

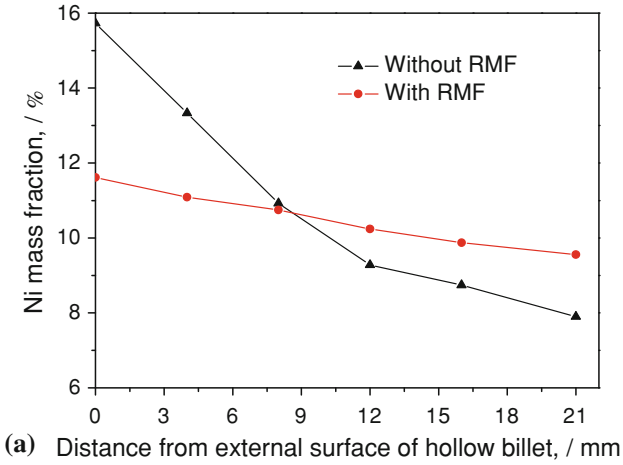

(a)

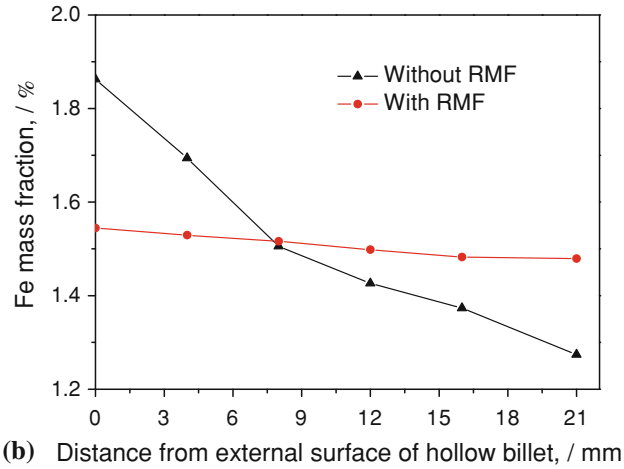

(b)

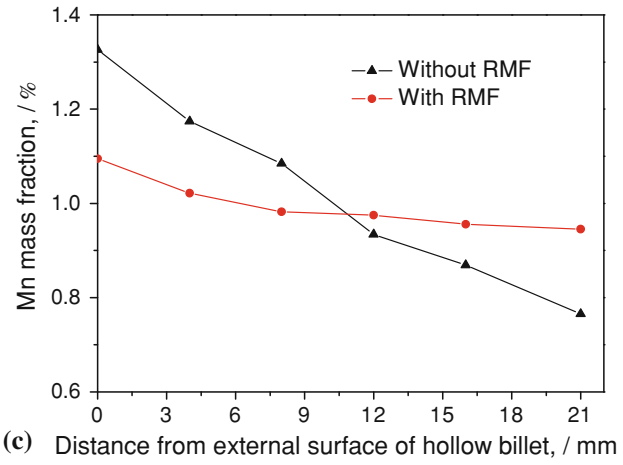

(c)

Fig. 6 Effect of RMF on macro-distribution of solute elements in CuNi10Fe1Mn alloy hollow billet: (a) Ni, (b) Fe, and (c) Mn

the liquid, and mushy zone. Thermosolutal convection and forced flow in the melt may aid or counteract the effects of ingot shape and melt entry on macrosegregation (Ref 3).

The positive segregation of solute elements along the radial direction results from the sequence solidification of horizontal continuous casting. The Ni, Fe, and Mn elements with higher melting point solidify in advance and are highly enriched on the dendrite arms at external surface and depleted at internal surface. Therefore, the contents of solute elements in melt reduce significantly along with solidification, which leads to the positive segregation. In the presence of RMF, the macrosegregation in the billet is significantly reduced.

Beckermann considers that the main mechanism of macrosegregation is the transport of solid and liquid phases in mushy zone (Ref 8). Nadella et al. (Ref 3) think that the relative movement between solid and liquid phases and the solute rejection by the solid phase are two essential conditions to form macrosegregation. However, there are many factors that control the macrosegregation extent of solute elements in CuNi10Fe1Mn alloy. It is considered that the grain refinement by RMF plays a significant role in segregation behavior.

Dahle and St. John (Ref 18) show in their study that a refinement of the grain size or a more globular morphology postpones dendrite coherency, at which the dendrites start to impinge on each other. The RMF results in greater grain refinement that more effectively postpones the structure coherency, which in turn retards the solidification that the time available for liquid flow through the interdendritic channels may be increased. The delayed structure coherency seems to allow a deeper penetration and have a longer time of the forced convection into the mushy zone with the corresponding washing out of the solute-rich liquid and the transport of this liquid to the internal surface (Ref 19). RMF also increases the relative movement between solid and liquid phases and accelerates the transport of solute elements that are rejected by the solid phase in mushy zone that decrease the macrosegregation. Moreover, with RMF, the applied RMF generates forced convection inside the melt will suppress the settling of solute-depleted dendrites in the sump.

4.3 Effect of RMF on Microsegregation of Solute Elements

The segregation ratio S_R is calculated by the following equation (Ref 20):

$$S_R = C_{\text{intergranular}}/C_{\text{intragranular}} \quad \text{(Eq 19)}$$

where $C_{\text{intergranular}}$ is the highest content of Ni element on intergranular; $C_{\text{intragranular}}$ is the lowest content of Ni element on intragranular.

During solidification of CuNi10Fe1Mn alloy, Ni and Fe elements usually concentrate on dendrites, and so they are negative segregation elements that the segregation ratios are less than 1; Mn element usually concentrates on interdendrite, and so it is a positive segregation element that the segregation ratio is more than 1. The effect of RMF on segregation ratios of solute elements is analyzed by EPMA, as shown in Fig. 7. The microsegregation of solute elements is reduced evidently by RMF, as seen from the figure.

The main reason for macrosegregation lies in microsegregation (Ref 3). It is well known that the solidification of alloys is accompanied by a certain degree of microsegregation of alloying elements due to their partitioning between liquid and solid phases during solidification, and due to the non-equilibrium nature of solidification. Although microsegregation (where diffusion distances are at the order of magnitude of the dendrite arm spacing or the cell size, usually between 10 and 100 μm) can be minimized or eliminated by heat treatments, microsegregation can significantly affect the homogenization time.

During solidification, solute is rejected to the solid-liquid interface of the grain. After the grains completely solidify, the

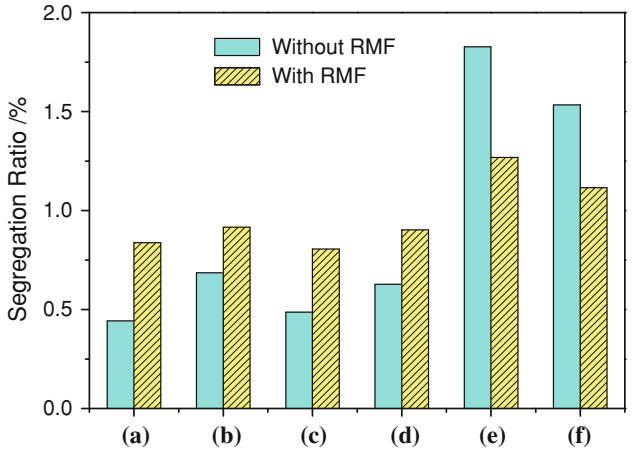

Fig. 7 Effect of RMF on segregation ratios of solute elements in CuNi10Fe1Mn alloy hollow billet: Ni element: (a) external surface, (b) internal surface; Fe element: (c) external surface, (d) internal surface; Mn element: (e) external surface, and (f) internal surface

grain boundary exhibits a high solute concentration. Dong et al. investigate the effect of a low-frequency electromagnetic field on the grain boundary segregation during DC casting of Al-Zn-Mg-Cu (7A60) alloy and found that the solubility of an alloying element inside the grain was effectively promoted (Ref 21). Therefore, RMF results in an increased solubility of Ni, Fe, and Mn elements in the Cu matrix during nonequilibrium solidification condition.

Element distribution is the process of atomic diffusion the diffusion extent of which can be estimated by the parameter α expressed below:

$$\alpha = D\frac{\tau}{l^2} \quad \text{(Eq 20)}$$

where D is the diffusion coefficient of solute, and τ is the diffusion time, namely, partial solidification time; l is the diffusion length that can be denoted by intragranular distance.

According to the Arrhenius equation, D can be denoted as

$$D = D_0 \exp(-Q/RT) \quad \text{(Eq 21)}$$

where D_0 is the diffusion constant; R is the gaseous constant; Q is activation energy; and T is the absolute temperature.

For example, with RMF, l is 3.28 μm at internal surface, τ is about 60 s, $D_{0,\,\mathrm{Ni}}$ is 2.3 $\mathrm{cm^2\ s^{-1}}$, Q_{Ni} is 242 $\mathrm{kJ\ mol^{-1}}$, R is 8.314 $\mathrm{J\ mol^{-1}\ K^{-1}}$, T is 1503 K. After calculation, the parameter α is about 4.9826. Without RMF, l is 9.17 μm at internal surface, and the other parameters are all the same. After calculation, the parameter α is about 0.6375. $\alpha_{\mathrm{Ni,\ with}}/\alpha_{\mathrm{Ni,\ without}} = 4.9826/0.6375 = 7.82$. From the calculation, it can be seen that the diffusion extent of Ni element with RMF is 7.82 times larger than that without RMF.

With the application of RMF, the grains are refined, and the range of the solute diffusion inside the grain is short which reduces the value of l. RMF retards the solidification time which increases the value of τ. The alternating electromagnetic field increased the entropy of the melt or the activation entropy which enhances the value of Q (Ref 21). Therefore, the microsegregations of Ni, Fe, and Mn elements are restrained remarkably.

The atoms will lose their electrons and become ions in liquid metals. The moving speed, v, of the ions is stochastic and free. Under an alternating electromagnetic field B, the speed v divides into two parts: $v_\perp$, perpendicular to the electromagnetic field: and $v_\parallel$, parallel to the electromagnetic field. A Lorentz force F results from the interaction between ions with charge q and electromagnetic field B (Ref 22, 23).

$$F = qv_\perp \times B \quad \text{(Eq 22)}$$

where F is perpendicular to $v_\perp$, and changes the direction of $v_\perp$, but does not change its magnitude, and so the ions go around the electromagnetic lines under the action of F. $v_\parallel$ forces ions to move in the direction of electromagnetic lines. The circum-rotation radius that the tracks of ions move along certain circles under the Lorentz force is as following (Ref 24):

$$r_c = \frac{mv_\perp}{B|q|} \quad \text{(Eq 23)}$$

From the above equation, it is seen that r_c is proportional to the mass of the ions, m, and inversely proportional to the charge, q. The radii of Cu^+, Ni^{2+}, Fe^{2+}, and Mn^{2+} are different for their differences in mass and charge, which results in a relative motion of the solute atoms and Cu atoms, and an increase in diffusion ability of the solute atoms in Cu matrix, and so the solubility of Ni, Fe, and Mn elements in Cu increases.

The relative and actual atomic weights of H atom are 1.00794 and 1.674×10^{-27} kg, respectively. The relative atomic weights of Cu, Ni, Fe, and Mn atoms are 63.546, 58.6934, 55.845, and 54.938045, respectively. Therefore, the actual atomic weights are 1.05538×10^{-25}, 9.74788×10^{-26}, 9.274811×10^{-26}, and $9.1241827 \times 10^{-26}$ kg, respectively. The electric quantity of an electron is 1.602×10^{-19} C. Therefore, the electrical quantity of Cu^+ is 1.602×10^{-19} C, and these of Ni^{2+}, Fe^{2+}, and Mn^{2+} are all 3.204×10^{-19} C. The range of magnetic induction acted on the electrons is from 22.3 to 28.5 mT. Hereby, the magnetic induction can be chosen to 25 mT in this calculation. According to Ref 25, the moving speed, v can be chosen to 0.2 $\mathrm{m\ s^{-1}}$ in this calculation. Therefore, the r_c values of Cu^+, Ni^{2+}, Fe^{2+}, and $Mn^{2+}$are 5.27, 2.43, 2.32, and 2.28 μm, respectively. Therefore, the values of r_c are on the micro-scale, and it is an effect on microsegregation. This may be another main factor that RMF reduces the microsegregation of solute elements.

Furthermore, in the presence of RMF, well-developed dendrite arms lead to a larger area of solid-liquid interface per unit volume. The amount of solute transferred by solid diffusion is proportional to the interface area. Therefore, the diffusion effect of solute elements is pronounced.

5. Conclusions

RMF makes the temperature field and liquid fraction uniform, promotes the grain refinement,and effectively restrains the macro/microsegregation of Ni, Fe, and Mn elements in horizontal continuous casting of CuNi10Fe1Mn alloy hollow billets. With RMF, the formerly inhomogeneous columnar grain macrostructure turns into homogeneous equiaxed grain structure, and the microstructures display different refined morphologies. The grain refinement by RMF plays a significant role in restraining the segregation behavior.

Acknowledgments

The authors gratefully acknowledge the support of the National Natural Science Foundation of China (Nos. 50274017 and 50674018).

References

1. J.P. Ault and G.A. Gehring, Jr., Statistical Analysis of Pitting Corrosion in Condenser Tube, *ASTM Spec. Tech. Publ.*, 1997, **3**, p 109–121
2. X.T. Li, X.W. Zhao, B. Wei, F.B. Chen, Z.M. Yan, and T.J. Li, Effect of Rotating Electromagnetic Field on Solidification Structures and Mechanical Properties of Tube Billets of BFe10-1-1 Alloy, *Chin. J. Nonferrous Met.*, 2007, **17**(6), p 922–926
3. R. Nadella, D.G. Eskin, Q. Du, and L. Katgerman, Macrosegregation in Direct-Chill Casting of Aluminium Alloys, *Prog. Mater. Sci.*, 2008, **53**, p 421–480
4. A.P. Boeira, I.L. Ferreira, and A. Garcia, Modeling of Macrosegregation and Microporosity Formation During Transient Directional Solidification of Aluminum Alloys, *Mater. Sci. Eng. A*, 2006, **435–436**, p 150–157
5. D.G. Eskin, R. Nadella, and L. Katgerman, Effect of Different Grain Structures on Centerline Macrosegregation During Direct-Chill Casting, *Acta Mater.*, 2008, **56**, p 1358–1365
6. S. Guo, Q. Le, Y. Han, Z. Zhao, and J. Cui, The Effect of the Electromagnetic Vibration on the Microstructure, Segregation, and Mechanical Properties of As-Cast AZ80 Magnesium Alloy Billet, *Metall. Mater. Trans. A*, 2006, **37**, p 3715–3724
7. I.L. Ferreira, C.A. Santos, V.R. Voller, and A. Garcia, Analytical, Numerical, and Experimental Analysis of Inverse Macrosegregation During Upward Unidirectional Solidification of Al-Cu Alloys, *Metall. Mater. Trans. B*, 2004, **35**, p 285–297
8. C. Beckermann, Modeling Segregation and Grain Structure Development in Equiaxed Solidification with Convection, *JOM*, 1997, **3**, p 13–17
9. T.J. Li, Z.Q. Cao, J.Z. Jin, and Z.F. Zhang, Control of Solidified Structure of Cast Metal by Imposing Electromagnetic Field, *Mater. Trans. JIM*, 2001, **42**, p 281–285
10. W.Z. Jin, F.D. Bai, T.J. Li, and G.M. Yin, Grain Refinement of Superalloy IN100 Under the Action of Rotary Magnetic Fields and Inoculants, *Mater. Lett.*, 2008, **62**, p 1585–1588
11. X.T. Li, Z.X. Guo, X.W. Zhao, and T.J. Li, Continuous Casting of Copper Tube Billets Under Rotating-Electromagnetic Field, *Mater. Sci. Eng. A*, 2007, **460-461**, p 648–651
12. Z.M. Yan, X.T. Li, Z.Q. Cao, X.L. Zhang, and T.J. Li, Grain Refinement of Horizontal Continuous Casting of the CuNi10Fe1Mn Alloy Hollow Billets by Rotating Magnetic Field (RMF), *Mater. Lett.*, 2008, **62**, p 4389–4392
13. X.S. Zheng, Y.C. Wang, Z.X. Li, and J.Z. Jin, Numerical Simulation of the Temperature Field in the Electromagnetic Semi-Continuous Casting of Slab, *Sci. Technol. Adv. Mater.*, 2001, **2**(1), p 109–111
14. T.T. Natarajan and N. El-Kaddah, Finite Element Analysis of Electromagnetic and Fluid Flow Phenomena in Rotary Electromagnetic Stirring of Steel, *Appl. Math. Model.*, 2004, **28**, p 47–61
15. X.T. Li, X.W. Zhao, X.R. Ma, and T.J. Li, Numerical Simulation of Solidification Process of Horizontal Continuously Cast BFe30-1-1 Hollow Billets, *Foundry*, 2007, **56**(8), p 841–844
16. D.Y. Ding and S.Q. Wu, Numerical Application of k-ε Turbulence Model to the Flow Over a Backward-Facing Step, *Sci. China Tech. Sci.*, 2010, **53**, p 2817–2825
17. C. Vives, Electromagnetic Refining of Aluminum Alloys by the CREM Process: Part I. Working Principle and Metallurgical Results, *Metall. Mater. Trans. B*, 1989, **20**(8), p 623–629
18. A.K. Dahle and D.H. St. John, Rheological Behaviour of the Mushy Zone and its Effect on the Formation of Casting Defects During Solidification, *Acta Mater.*, 1998, **47**(1), p 31–41
19. T.L. Finn, M.G. Chu, and W.D. Bennon, *Micro/Macro Scale Phenomena in Solidification*, C. Beckermann, L.A. Bertram, S.J. Pien, and R.E. Smelser, Ed., ASME, New York, 1992, p 17–26
20. H.Q. Hu, *Metal Solidification Principle*, 2nd ed., China Machine Press, Beijing, 2000
21. J. Dong, J.Z. Cui, F.X. Yu, C.Y. Ban, and Z.H. Zhao, Effect of low-Frequency Electromagnetic Casting on the Castability, Microstructure, and Tensile Properties of Direct-Chill Cast Al-Zn-Mg-Cu Alloy, *Metall. Mater. Trans. A*, 2004, **35**, p 2487–2494
22. Z.C. Han, *Electromagnetic Metallurgy*, Metallurgical Industry Press, Beijing, 2001
23. J.Z. Cui, Solidification of Al Alloys Under Electromagnetic Field, *Trans. Nonferrous Met. Soc. Chin.*, 2003, **13**, p 473–483
24. J.L. Xu and S.X. Jin, *Plasma Physics*, Atom Energy Press, Beijing, 1981
25. J. Li, T. Wang, J. Xu, Z. Yan, J. Sun, J. Xu, Z. Cao, and T. Li, Simulation Study on Horizontal Continuous Casting Process of Copper Hollow Billet Under Rotating Electromagnetic Stirring. Part 1: Model Description and Primary Results, *Mater. Sci. Techol.*, 2009, doi: 10.1179/026708309X12535382371933